Modulated roll cells in rotating plane Couette flow of viscoelastic fluid

Tomohiro Nimura
Department of Mechanical Engineering,
Tokyo University of Science
Yamazaki 2641 Noda, Chiba 278-8510, Japan
nimura8t@gmail.com

Takahiro Ishida
Department of Mechanical Engineering,
Tokyo University of Science
Yamazaki 2641 Noda, Chiba 278-8510, Japan

Takuya Kawata
Department of Mechanical Engineering,
Tokyo University of Science
Yamazaki 2641 Noda, Chiba 278-8510, Japan
kawata@rs.tus.ac.jp

Takahiro Tsukahara*
Department of Mechanical Engineering,
Tokyo University of Science
Yamazaki 2641 Noda, Chiba 278-8510, Japan
tsuka@rs.tus.ac.jp

ABSTRACT
In order to understand the (polymer-induced) drag-reduction mechanism in wall turbulence of viscoelastic fluid, it must be crucial to elucidate how the viscoelasticity modulates the streamwise-elongated vortical structure, which is a characteristic feature in the near-wall turbulence. In the present study we numerically study the roll-cell structure of laminar rotating plane Couette flow of viscoelastic fluid, aiming at further understanding the effect of viscoelasticity on the longitudinal vortices in shear flow. The case of $Re = 25$ and $Ro = 0.4$ is focused as a typical state that provides two-dimensional steady roll cells for the Newtonian fluid case, and we investigate how such two-dimensional vortices would be modulated by the viscoelasticity at different Weissenberg numbers. The viscoelasticity is found to give rise to an unsteady flow state where the two-dimensional roll-cell structure is periodically strengthened and suppressed with the time scale of the relaxation time of the fluid viscoelasticity. Such a pulsatile fluid motion was caused by the delay in the response of the viscoelastic force to the change in the velocity gradient, and the effect of the viscoelasticity to the momentum transport in the flow field is also discussed in detailed.

INTRODUCTION
The drag reduction effect by adding polymer or surfactant into a liquid turbulent flow has been studied for many years since its discovery in the 1940s (Toms, 1948). Recent studies by means of experiments and direct numerical simulations (DNS, Sureshkumar et al., 1997) have revealed that stretched polymer molecules by turbulent motions would cause a high extensional viscosity and suppress turbulent eddies, and some researchers also proposed a mechanism of drag reduction in terms of energy storage and release by the polymer molecules or surfactant micellar networks (Procaccia et al., 2008). However, the mechanism of the drag reduction effect remains still ambiguous due to complexities of viscoelastic effect as well as turbulence. Modulation of coherent streamwise vortical structures in the near-wall region of wall turbulence is considered as a key phenomenon to understand the drag-reduction mechanism of the viscoelastic wall-bounded turbulent flow.

Plane Couette flow subject to spanwise system rotation (rotating plane Couette flow, RPCF), the definition of which is schematically shown in Fig. 1, is known to have distinct coherent streamwise roll cells and can, therefore, be a good test case to study the effect of viscoelasticity on longitudinal vortices in a wall-bounded shear flow. In the case of anti-cyclonic system rotation, where the system is rotating in the opposite direction to the wall shear, the flow is linearly unstable due to the Coriolis force effect, which gives rise to streamwise-elongated roll-cell structure. Depending on the Reynolds number and the system rotation rate, the coherent roll cells take various types of form, such as two-dimensional steady roll cells and three-dimensional wavy roll cells (Tsukahara et al., 2010; Kawata and Alfredsson, 2016a; 2016b). Comparing the flow structure of this flow for Newtonian and viscoelastic fluid one may gain physical insight into how the viscoelasticity modulates longitudinal vortices in shear flow.

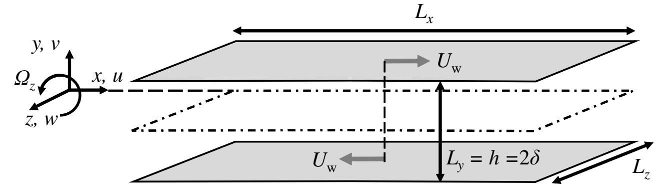

Figure 1. Definition of the RPCF and the coordinate system.

In this work we perform a parametric DNS study of the viscoelastic RPCF systematically changing three flow parameters, i.e., the Reynolds number Re, the rotation number Ro, and the Weissenberg number Wi (the definitions of these parameters are given in the next section). The laminar case of $Re = 25$ and $Ro = 0.4$ is focused as a typical state accompanied by steady two-dimensional roll cells that appear for the Newtonian fluid, and the modulated flow structures for viscoelastic fluid are compared at different values of Wi. It is shown that the addition of the viscoelasticity gives rise to the unsteady flow state where the two-dimensional roll cells are periodically strengthened and suppressed. The mechanism of such periodic unsteadiness is addressed in detailed, and it is also discussed how such a change in the flow states by the viscoelasticity affects the momentum transport (Dubief et al., 2004) in the flow field.

DIRECT NUMERICAL SIMULATION

Flow System
The coordinate system is defined as shown in Fig. 1: the x-, y-, and z-axes are taken in the streamwise, wall-normal and spanwise directions, respectively. The top and bottom walls are located at $y =$

[1]Corresponding author.

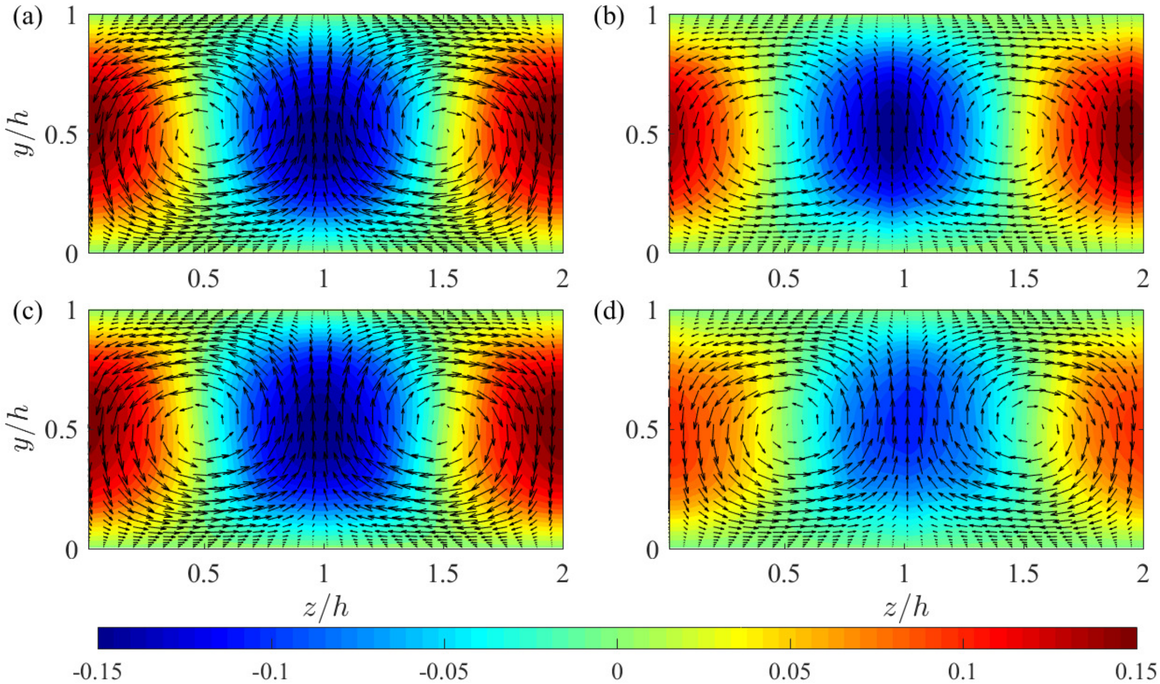

Figure 2. Comparison of the roll-cell structure of the RPCF at $Re = 25$ and $Ro = 0.4$ for (a) the Newtonian fluid and (b-d) the viscoelastic fluid with three different Wi: (b) $Wi = 500$, (c) $Wi = 1000$, (d) $Wi = 2000$. The colour indicates fluctuations in the streamwise velocity u'/U_w and the black arrows show the pattern of the cross-flow vector (v, w). $2h$ length of the arrows corresponds to velocity magnitude of U_w.

h and $y = 0$, respectively, and they are moving in opposite direction with speed U_w. The Reynolds number Re and the rotation number Ro are defined, based on the wall speed U_w and the half channel height $\delta(= h/2)$, as $Re = U_\mathrm{w}\delta/\nu$ and $Ro = 2\Omega_z\delta/U_\mathrm{w}$, respectively, where ν is kinematic viscosity at zero shear rate.

Governing Equations and Numerical Procedure

The governing equations numerically solved in the present DNS are the non-dimensional continuity equation and the Navier-Stokes equation written on the frame rotating with the system:

$$\frac{\partial u_i^*}{\partial x_i^*} = 0, \tag{1}$$

$$\frac{\partial u_i^*}{\partial t^*} + u_j^*\frac{\partial u_i^*}{\partial x_j^*} = -\frac{\partial p^*}{\partial x_i^*} + \frac{\beta}{Re}\frac{\partial^2 u_i^*}{\partial x_j^{*2}} - Ro\,\varepsilon_{i3k}u_k^* + \frac{1-\beta}{Wi}\frac{\partial c_{ij}}{\partial x_j^*}. \tag{2}$$

Here, p is the pressure, ε_{ijk} is the Levi-Civita symbol, and the variables with the superscript $*$ stand for the non-dimensional quantities normalised by δ and/or U_w. The non-dimensional parameters of the viscosity ratio and the Weissenberg number are defined as $\beta = \mu_\mathrm{s}/(\mu_\mathrm{s} + \mu_\mathrm{a})$ and $Wi = U_\mathrm{w}^2\lambda/\nu$, where μ_s and μ_a are the viscosity of the solution and the additive, respectively, and λ is the relaxation time of the additive. The Weissenberg number Wi physically represents the ratio of the relaxation time of the additive to the viscous time scale. The conformation tensor c_{ij} of the last term in Eq. (2) is the viscoelastic stress, which is governed by a constitutive equation. We adopted the Giesekus model (Giesekus, 1982):

$$\begin{aligned}\frac{\partial c_{ij}}{\partial t^*} &+ \frac{\partial u_m^* c_{ij}}{\partial x_m^*} - \frac{\partial u_i^*}{\partial x_m^*}c_{mj} - \frac{\partial u_j^*}{\partial x_m^*}c_{mi} \\ &+ \frac{Re}{Wi}\left[c_{ij} + \alpha(c_{im} - \delta_{im})(c_{mj} - \delta_{mj}) - \delta_{ij}\right] = 0,\end{aligned} \tag{3}$$

where α is the mobility factor. In the present study, the viscosity ratio and the mobility factor are fixed at $\beta = 0.8$ and $\alpha = 0.001$.

We employed the finite difference method for the spatial discretization. The forth-order central difference scheme was used for the x- and z-directions, while the second-order central difference scheme was adopted in the wall-normal (y-) direction. For the time integration, the second-order Crank-Nicolson and the second-order Adams-Bashforth schemes were used for the wall-normal viscous term and the other terms, respectively. As for the boundary condition, the periodic boundary conditions were imposed in the x and z directions and the non-slip condition was applied on the walls. The computational domain size ($L_x \times L_y \times L_z$) was $7.5h \times h \times 2h$ and the grid number was 128 in all directions.

As already stated, we focus on the case only of $Re = 25$ and $Ro = 0.4$ in the present paper, and the DNS results for several different Weissenberg numbsers in a range of $Wi = 0$–2000 are compared.

RESULTS

Figure 2 presents the cross-sectional view of flow structures observed in the laminar RPCFs of Newtonian fluid and viscoelastic fluids for each Wi. The contour indicates the fluctuation magnitude of the streamwise velocity component u'/U_w and the arrows represent the pattern of cross-flow vectors (v, w). Note that the mean components of v and w are nought in the present flow system. The length of $2h$ of the black arrows corresponds to the velocity magnitude of U_w. As shown in the figure, a large-scale roll-cell structure with the size of channel gap clearly appears for all cases, and the secondary motion of the roll cells induces the periodic spanwise variation of streamwise velocity of about 15% of the wall speed U_w. It also should be noted that all these observed structures are two-dimensional, i.e., straight infinitely in the streamwise direction.

Although the spatial structures that appear in these four cases are quite similar to each other, the significant difference is seen in

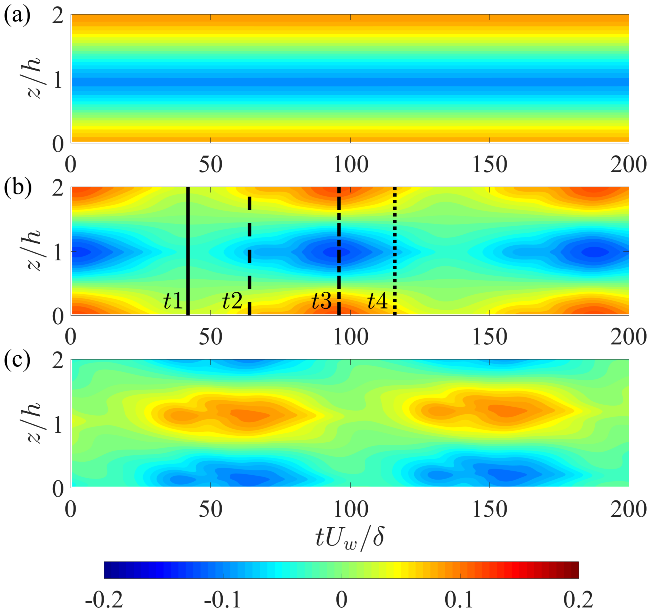

Figure 3. Space-time diagrams of fluctuations in the streamwise velocity u/U_w on the channel centreline $y/h = 0.5$ for the viscoelastic fluid cases: (a) $Wi = 500$, (b) $Wi = 1000$, (c) $Wi = 2000$. The black lines in the panel (b) represent the instances depicted for the later analysis.

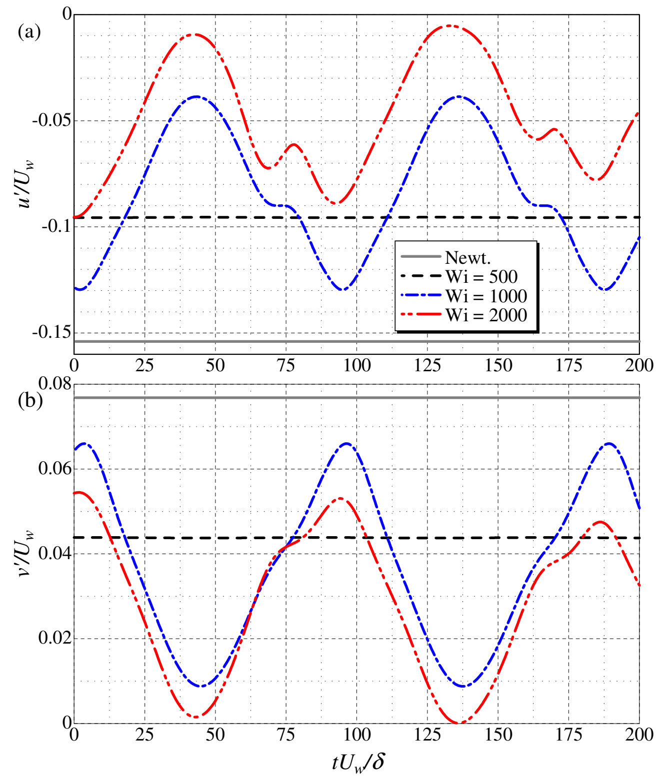

Figure 4. Time sequence of fluctuations in (a) the streamwise velocity u'/U_w and (b) the wall-normal velocity v'/U_w at channel centre ($y/h = 0.5$). Each four lines indicate Newtoinan fluid and different Wi.

their temporal behaviours. Figure 3 presents space-time diagrams (z-t diagram) of u'/U_w on the centreline of the channel at an arbitrary streamwise position for the viscoelastic fluid cases. From the diagram, one may find a pair of positive and negative regions that alternate in the spanwise direction. These regions correspond to streaks induced by streamwise roll cells. In the case of Newtonian fluid, the two-dimensional roll cells are steady (not shown in the figure) and, hence, is similar with the case of the present smallest Weissenberg number $Wi = 500$ given in Fig. 3(a), where one may see the position and magnitude of streaks do not change in time. On the other hand, for the cases of higher Weissenberg numbers shown in Figs. 3(b) and (c), the periodic variations of the streamwise velocity are clearly confirmed. It is also seen here that despite significant variation of the magnitude the velocities does not change the sign; for example, at $z/h = 1$ in the panel (c) u' is always negative, while the magnitude significantly changes in time. Therefore, the flow structure only repeats being strengthened and weakened periodically without altering the sign.

More details of such 'pulsatile motion' of the structure are presented in Fig. 4, in which the time series of the streamwise and wall-normal velocities at $z/h = 1.0$ of Fig. 3 are compared for different Weisseberg numbers. As shown in the figure, in the cases of Newtonian fluid and $Wi = 500$ both of the velocity components are constant in time, while in the higher Weissenberg number cases significant periodic variations can be seen. The amplitude of the pulsatile variation is approximately 10% and 5% of the wall speed U_w for u' and v', respectively. It is also seen that in the phase where u' is decreasing (and v' is increasing) the variation is not monotonic, which can be typically seen at around $tU_\mathrm{w}/\delta = 75$ and 175, and such deviation from simple sinusoidal curve is more significant for higher Weissenberg number case.

One can also see that the period of the pulsatile motion is significantly long compared to the time scale of the wall shear, about $100tU_\mathrm{w}/\delta$ in both cases. As the relaxation time of the additive in terms of the wall-shear time scale is $\lambda/(\delta/U_\mathrm{w}) = Wi/Re = 40$, and 80 for $Wi = 1000$ and 2000, respectively, this period of the pulsatile motion is on the order of the relaxation time. It also should be noted here that between the cases of $Wi = 1000$ and 2000 the period of the pulsatile fluid motion is not changed although the relaxation time is doubled.

Comparing the mean value of the velocities shown in Fig. 4, one can see that the magnitude of the velocities decrease as the Weissenberg number increases. In the case of $Wi = 500$ both the magnitudes of u' and v' are significantly decreased compared to those in the case of Newtonian fluid, and also for higher Wi cases the velocity magnitude decreases as Wi increases. This means that by the addition of viscoelasticity the spatial variation of the velocities caused by the flow structure is weakened.

Figure 5 represents variation of the skin-friction coefficient as a function of Wi. The values of C_f were obtained as the mean streamwise-velocity gradient on the wall that are averaged in the streamwise and spanwise directions and in time. It can be seen that C_f decreases with increasing Wi. The C_f value for $Wi = 2000$ decreases by 10% of that of the Newtonian fluid case. Such a decrease in C_f indicates that the momentum transport by the flow structure is weakened by the viscoelasticity, which is consistent with the tendency observed in the time series of velocities in Fig. 4.

Now, we pick up four representative instances in the pulsatile change of flow structure for $Wi = 1000$ that are defined in Fig. 3(b) with black vertical lines. The time instants $t = t_1$ and t_3 are moments when the spanwise variation of fluctuations in u'/U_w on the channel centreline is least and most significant, respectively, whereas t_2 and t_4 are those when the trace of the viscoelastic stress tensor $c_{11} + c_{22} + c_{33}$ become minimum and maximum, respectively. Figure 6 shows the spatial two-point correlation function of the wall-normal

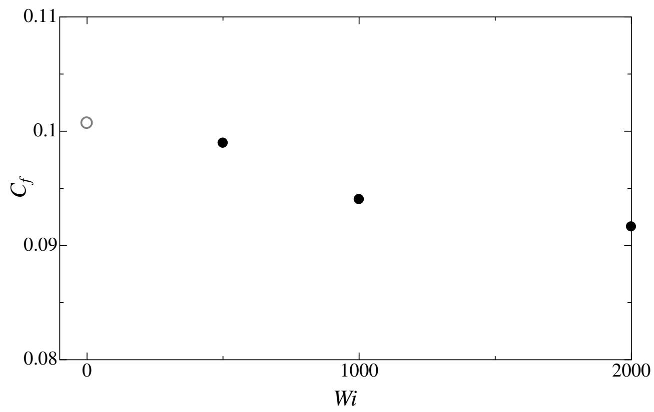

Figure 5. Effect of viscoelasticity on the skin friction coefficient.

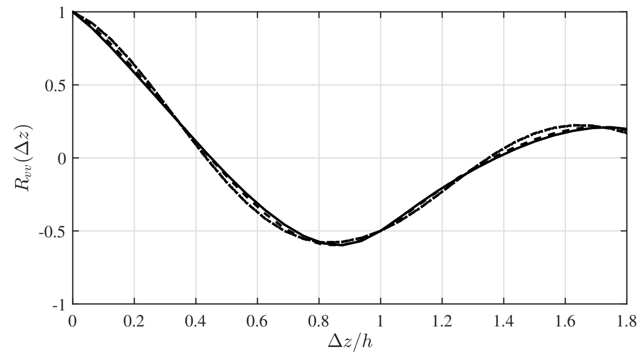

Figure 6. Spanwise spatial two-point correlation function of the wall-normal velocity $C_{vv}(\Delta z)$ on the channel centreline for $Wi = 1000$. The profile of $C_{vv}(\Delta z)$ is plotted for four different instances $t = t_1$, t_2, t_3, and t_4 shown in Fig. 3(b) by the corresponding white lines.

velocity v on the channel centreline at these moments, and it can be easily seen that the profiles of $R_{vv}(\Delta z)$ are almost identical to each other, indicating that during the pulsatile variation of roll cells only the magnitude of the vortical structure are varied in time, while the 'shape' of the roll-cell structure, such as the spanwise width of the roll cells, keeps unchanged.

Cross-sectional views of the roll-cell structure at these instances are presented in Fig. 7. Each column of the figure array gives the distributions of (a1–4) velocities, (b1–4) viscous forces, and (c1–4) viscoelastic forces at $t = t_1$, t_2, t_3, and t_4 from the top to the bottom. In the panels (a1–4), the fluctuating streamwise velocity u'/U_w is shown by the contour and the cross-flow vectors are shown by the black arrows. It is seen that the roll-cell structure is strengthened from (a1) to (a3) and weakened again in (a4). In the panels (b1–4), the streamwise viscous force is shown by the contour and the black arrows represent the in-plane viscous force vectors. Comparing the panels (b1–4) to (a1–4), one can see that the distribution of the in-plane viscous force is counterrotating against the secondary motion of the roll cells, and the positive/negative peak of the streamwise viscous force corresponds to the negative/positive peak of the fluctuating streamwise velocity, indicating that the viscous force is always counteracting the flow structure.

In the panels (c1–4) of Fig. 7, the streamwise normal component of the viscoelastic stress tensor c_{11} is shown by the contour, and the white arrows represent the in-plane viscoelastic force (E_2, E_3), where

$$E_2 = \frac{1-\beta}{Wi}\left(\frac{\partial c_{22}}{\partial y^*} + \frac{\partial c_{23}}{\partial z^*}\right),\ E_3 = \frac{1-\beta}{Wi}\left(\frac{\partial c_{32}}{\partial y^*} + \frac{\partial c_{33}}{\partial z^*}\right). \quad (4)$$

The streamwise normal viscoelastic stress c_{11} is dominant in the trace of the viscoelastic stress tensor c_{ii} in this flow, and the physical meaning can be interpreted as the polymer stretching in the streamwise direction. It is seen that c_{11} is almost zero inside the roll cells while it increases on the edge of the roll cells, e.g., at $z/h = 0$, 1 and 2 of Fig. 7. A similar tendency can be observed for the in-plane viscoelastic force distribution. In particular, comparing with the in-plane viscous force at the same instance, one can see that magnitude of the viscoelastic force is generally smaller than the viscous force inside the roll cells (the viscous and viscoelastic forces in the panels (b1–4) and (c1–4) are shown with the same length unit scale of the arrows), while on the edges of the roll cells the viscoelastic force is as large as the viscous force.

Such tendency in behaviour of the viscoelastic force is more easily seen in Fig. 8, where the region around $(z/h, y/h) = (1, 0.5)$ of Fig. 7(b4) and (c4) are magnified. Inside the roll cells, the white arrows in the bottom figure representing the viscoelastic force are clearly shorter compared to the black arrows of the viscous force in the top figure, while on the edge of the roll cell (around $z/h = 1$) the white arrows are longer than the black arrows. It also should be noted that in the region of $0.2 \le y/h \le 0.4$ around $z/h = 1$ the viscoelastic force is in the same direction as the cross flow pattern. Such tendency supporting the secondary motion of the roll-cell structure cannot be observed for the viscous force, and this can be an important difference in behaviour of the viscous force and the viscoelastic force.

The other noteworthy tendency here is the delay in the response of the viscoelastic force to the variation of the flow structure: while the roll-cell structure and the viscous force become most significant at $t = t_3$, it is $t = t_2$ when the viscoelastic force becomes most largest. Such time lag between the variation of flow field and the viscoelastic tensor is shown more detailed in Fig. 9, where the time series of the kinematic energy and the trace of the viscoelastic stress tensor integrated over the cross section of the channel, $K = \int_0^{2h}\int_0^h (u^2+v^2+w^2)/2\mathrm{d}y\mathrm{d}z$ and $C_{ii} = \int_0^{2h}\int_0^h (c_{11}^2+c_{22}^2+c_{33}^2)\mathrm{d}y\mathrm{d}z$, are presented for the cases of $Wi = 1000$ and 2000. In both cases, one can clearly seen there exist significant delay between the temporal variation of K and C_{ii}. In order to quantify the time delay between the flow structure and the viscoelastic stress, the temporal cross correlation between the time series of K and C_{ii} are evaluated and shown in Fig. 10(a) for three different Wi cases. For all the cases, the cross correlation between K and C_{ii} at $\Delta t = 0$ is negative, and the first positive peak of cross correlation is located at $t/\lambda = Re/Wi \cdot t^* = 1.5$, 0.81, and 0.34 for $Wi = 500$, 1000, and 2000, respectively. This indicates the time delay between the flow structure and viscoelastic stress is on the order of the relaxation time λ, although it still cannot be scaled well only by λ.

In order to shed light on the energy transfer between the flow structure and the additive (polymer) of the viscoelastic fluid, the energy transfer term between the kinetic energy of the flow field and the 'elastic' energy of the polymer is focused. The kinetic-energy transport equation is written as

$$\begin{aligned}\frac{\mathrm{D}k}{\mathrm{D}t} = \frac{\partial u_i p}{\partial x_i} + \frac{\beta}{Re}\nabla^2 k - \frac{\beta}{Re}\left(\frac{\partial u_i}{\partial x_j}\right)^2 \\ + \frac{1-\beta}{Wi}\left(\frac{\partial u_i c_{ij}}{\partial x_j} - c_{ij}\frac{\partial u_i}{\partial x_j}\right),\end{aligned} \quad (5)$$

and one can see that $c_{ij}\partial u_i/\partial x_j$ in the right-hand side appears also

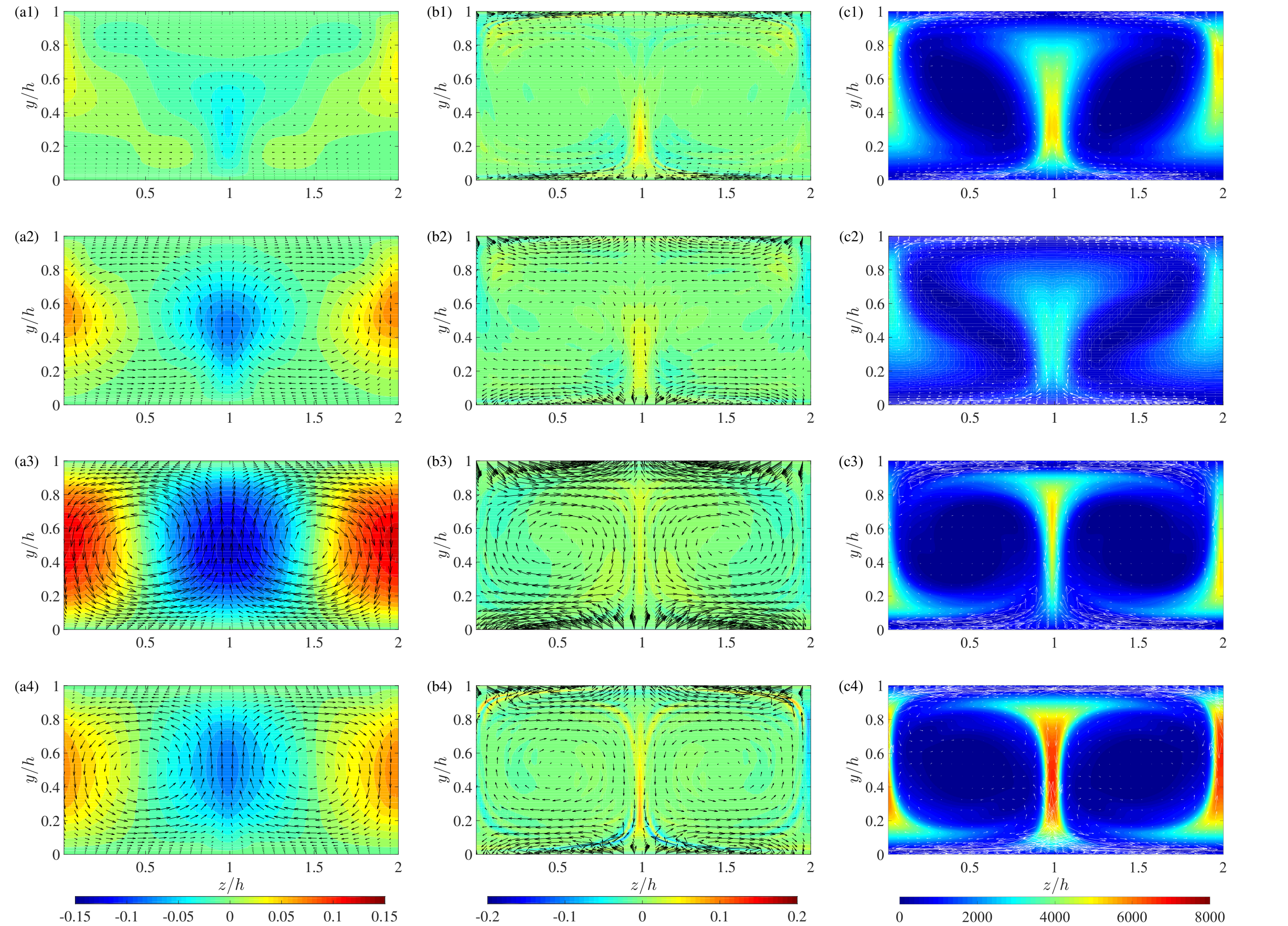

Figure 7. Temporal evolution of (a1-4) velocity field, (b1-4) viscosity force field, (c1-4) vicoelastic force field on arbitrary cross-sectional plane for $Wi = 1000$. The column of the figure array indicates the time evolution; (a-c1), (a-c2), (a-c3), and (a-c4) present the distributions at $t = t_1$, t_2, t_3, and t_4, respectively, that are defined in Fig. 3(b). The colours and the arrows in the figures represent; (a1-4) the same as in Fig. 2, (b1-4) the streamwise component and in-plane components of the viscous force vector, respectively; (c1-4) the streamwise normal component of the viscoelastic stress tensor c_{11} and in-plane components of the viscoelastic force vector (E_2, E_3), respectively.

in Eq. (3) with opposite sign, which indicates that this term physically represents the energy transfer between k and c_{ii}. Integrating Eq. (5) over the cross section of the channel, one obtains the equation for K:

$$\frac{\mathrm{d}K}{\mathrm{d}t} = \frac{\beta}{Re}\int_0^{2h}\left(-\left.\frac{\partial k}{\partial y}\right|_{y=0} - \left.\frac{\partial k}{\partial y}\right|_{y=h}\right)\mathrm{d}z - \frac{\beta}{Re}\iint\left(\frac{\partial u_i}{\partial x_j}\right)^2 \mathrm{d}S - \Psi_{ii}, \tag{6}$$

where $\Psi_{ii} = \iint c_{ij}\partial u_i/\partial x_j \mathrm{d}S$ is the integrated energy transfer term. As can be seen from Eq. (6), if not for the viscoelasticity the kinetic energy is maintained by the balance between only the viscous diffusion term (the first term) and the viscous dissipation term, whereas in the case of the viscoelastic fluid the energy transfer term Ψ_{ii} comes into play.

Figure 10(b) shows the temporal cross-correlation function between K and Ψ_{ii}. It is seen that the cross correlation is almost unity at $\Delta t = 0$, which means that there is no time delay between the temporal variation of K and Ψ_{ii}. If the kinetic energy of the flow structure increases, the energy is forthwith transferred to the additive though the energy transfer term Ψii. However, the viscoelastic stress does not response immediately. There is a certain time delay on the order of the relaxation time of the additive before the viscoelastic stress reacts, as mentioned above. This delay in the response of the viscoelastic force gives rise to unsteady periodic variation with the time scale of the relaxation time.

CONCLUSION

We numerically investigated flow structure of laminar rotating plane Couette flow of viscoelastic fluid by means of DNS. The case of $Re = 25$ and $Ro = 0.4$ was focused with a particular interest in how two-dimensional steady roll-cell structure that appears in the Newtonian fluid case is modulated by the addition of the viscoelasticity. The viscoelasticity was found to give rise to unsteady flow state in the case of large enough Weissenberg number, where only the amplitude of two-dimensional roll cells is periodically strengthened and suppressed without significant change in the spatial structure. In the cases of such pulsatile flow state the mean magnitude of the flow structure is suppressed and the skin friction is reduced compared to the steady flow states. The viscoelastic force is found to partly support the secondary motion of the roll cells, unlike the

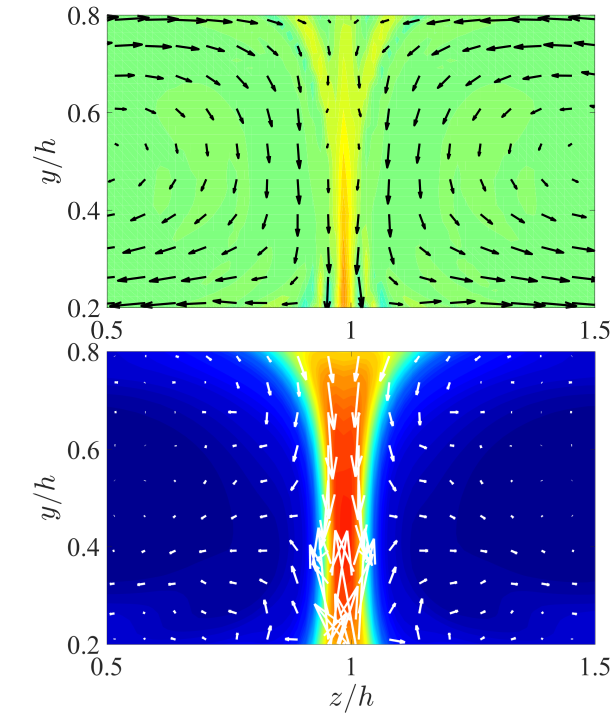

Figure 8. Magnified view of the region around $(z/h, y/h) = (1, 0.5)$ in (top) Fig. 7(b4) and (bottom) Fig. 7(c4). The contour and the length scale of the white arrows are the same as in the original fiugres.

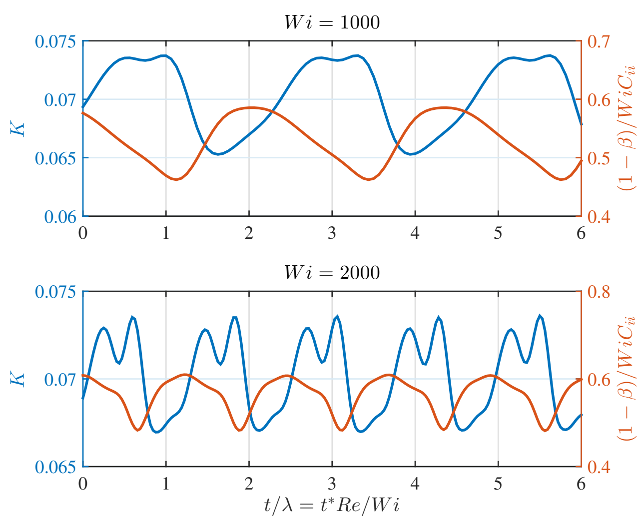

Figure 9. Time sequence of the kinetic energy and the trace of the viscoelastic stress tensor integrated across the cross section of the channel for (top) $Wi = 1000$ and (bottom) $Wi = 2000$.

viscous force that is always counteracting to the roll cells. There is a certain time delay in the temporal variation of the kinetic energy of the flow structure and the response of the viscoelastic stress to it. Such time delay is found to be on the same order as the relaxation time of the fluid viscoelasticity but is not perfectly scaled with it. The present results indicates that energy exchange between the flow structure and the viscoelasticity of fluid that occurs with a time scale much longer than those of shear and viscosity gives rise

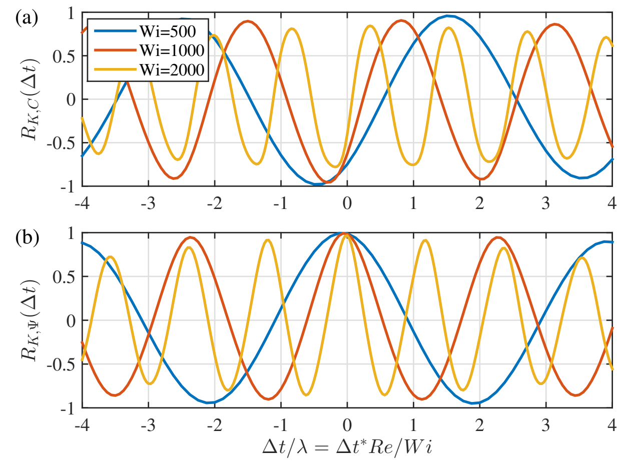

Figure 10. Temporal two-point cross-correlation function between (a) the integrated kinetic energy K and the integrated trace of the viscoelastic stress tensor C_{ii}, (b) K and the integrated energy transfer term Ψ_{ii} for three different Weissenberg number: blue, $Wi = 500$; red, 1000; yellow, 2000.

to unsteady flow state, which may have significant impact on the momentum transport of the flow field.

REFERENCES

Dubief, Y., White, C. M., Terrapon, V. E., Shaqfeh, E. S., Moin, P., & Lele, S. K., 2004, On the coherent drag-reducing and turbulence-enhancing behaviour of polymers in wall flows, J. Fluid Mech., 514, 271–280.

Giesekus, H., 1982, A simple constitutive equation for polymer fluids based on the concept of deformation-dependent tensorial mobility, J. Non-Newtonian Fluid Mech., 11(1-2), 69–109.

Kawata, T., & Alfredsson, P. H., 2016a, Experiments in rotating plane Couette flow—momentum transport by coherent roll-cell structure and zero-absolute-vorticity state, J. Fluid Mech., 791, 191–213.

Kawata, T., & Alfredsson, P. H., 2016b, Turbulent rotating plane Couette flow: Reynolds and rotation number dependency of flow structure and momentum transport, Phys. Rev. Fluids, 1(3), 034402.

Procaccia, I., L'vov, V. S., & Benzi, R., 2008s, Colloquium: Theory of drag reduction by polymers in wall-bounded turbulence, Reviews of Modern Physics, 80(1), 225–247.

Sureshkumar, R., Beris, A. N., & Handler, R. A., 1997, Direct numerical simulation of the turbulent channel flow of a polymer solution, Phys. Fluids, 9(3), 743–755.

Toms, B. A., 1948, Some observations on the flow of linear polymer solutions through straight tubes at large Reynolds numbers, In Proceedings of the 1st International Congress on Rheology 2, 135–141.

Tsukahara, T., Tillmark, N., Alfredsson, P.H., 2010, Flow regimes in a plane Couette flow with system rotation, J. Fluid Mech., 648, 5–33.